Journal of Marine Science and Application (2026) 25: 393-402
https://doi.org/10.1007/s11804-025-00691-8

RESEARCH ARTICLE

Numerical Simulation and Characteristic Analysis of Water Entry Cavitation in Limited-Domain Water

Ming He[1], Yexian Wang[1], Enfan Lin[1], Wenzhi Cui[1] and Jiale Yan[1,2]

Received: 02 January 2025 / Accepted: 23 February 2025

Abstract

Structural water entry remains a significant issue in fluid mechanics. Technological advancements and the diversification of application scenarios have introduced complex environmental boundaries, including irregular fluid and limited-domain boundaries, which are encountered during water entry. This study employs the Eulerian finite element method to simulate fluid dynamics and applies an improved immersed boundary method to address problems involving fluid–structure interaction interfaces. A coupled numerical model for structural water entry in limited-domain water is developed. Initially, a theory of water entry cavitation is derived, and the approximate range of boundary effects is determined. Results of pressure regulation experiments show that the numerical model fully demonstrates the numerical algorithm's effectiveness. Therefore, numerical methods are used in comprehensively analyzing the effects of structural size, water domain size, and water entry speed. Modifications to these factors can alter cavitation evolution characteristics, influencing a structure's motion state by qualitatively revealing the physical mechanisms of the process through the evolution of free surfaces, speed attenuation, and acceleration evolution at varying parameters. The findings provide valuable technical support for future navigation design.

Keywords Water entry; Fluid–structure interaction; Limited-domain; Eulerian finite element method; Immersed boundary method

1 Introduction

Research on structural water entry has a long history (Howison et al., 1991; Aristoff and Bush, 2009; Truscott et al., 2014; Prasad et al., 2024) and remains a prominent topic in fluid mechanics, finding extensive applications in military, civilian, and natural science domains. Investigating the intricate mechanical aspects of structural water entry constitutes the core of technical research and development for cross-medium missiles (Zhang et al., 2021; Zhang et al., 2022), supercavitating vehicles (Yuan et al., 2012; Zou and Gan, 2024), and spacecraft return capsule recovery (Zhang et al., 2017). Transient impact loads, cavitation evolution, free surface fragmentation, and motion trajectory are the essential physical attributes of structural water entry, encompassing multiphase and multiscale fluid–structure interaction characteristics. Despite advancements in these areas, considerable challenges remain.

Previous studies have comprehensively addressed structural water entry through theoretical research, experimental research, and numerical simulation. Theoretical research has demonstrated the benefits of solving straightforward problems. Karman (1929) initially investigated the collision of seaplanes during landing from a theoretical perspective. Wagner (1932) expanded the theory of Karmon (1929) by accounting for splashing and free surface formation. Logvinovich (1969) introduced the concept of independent cavitation expansion based on potential flow theory, methodically explaining the flow characteristics of super cavities around slender bodies. Lee et al. (1997) applied the principle of energy conservation to study cavitation evolution dynamics during high-speed projectile water entry, developing a theoretical model for cavitation evolution. Lastly, a previously proposed cavitation equation (Zhang et al., 2024) provided theoretical guidance for predicting water entry cavitation.

Article Highlights

- This study employs the Eulerian finite element method to simulate fluid dynamics and applies an improved immersed boundary method to address problems involving fluid–structure interaction interfaces.
- An effective coupled numerical model for structural water entry in limited-domain water is developed.
- Some special flow mechanisms have been revealed, including unstable fluctuations in free surface.

✉ Jiale Yan
jialeyan@pku.edu.cn

[1] State Key Laboratory for Turbulence and Complex Systems, Department of Mechanics and Engineering Science, BIC-ESAT, College of Engineering, Peking University, Beijing 100871, China

[2] Laoshan Laboratory, Qingdao 266237, China

Experimental research has been proven invaluable in studying water entry phenomena. Worthington and Cole (1899) utilized a camera to examine a sphere's vertical water entry, analyzing a free surface's evolution and cavitation closure on the basis of experimental results. Gekle et al. (2009) conducted experiments on disk water entry, focusing on the flow characteristics of gases inside a cavitation structure during necking and deep closure. Aristoff and Bush (2009) identified four closure modes for cavitation around superhydrophobic spheres: surface closure, deep closure, shallow closure, and quasistatic closure. Truscott and Techet (2009) examined the cavitation and motion characteristics of sphere water entry at varying angular velocities, analyzing the results for hydrophilic and hydrophobic spheres through high-speed photography.

Numerical simulation (Huang et al., 2022; Zhang et al., 2022) is the primary research method employed in this study, and previous researchers have made significant progress in this field. Iranmanesh and Passandideh-Fard (2017) developed a three-dimensional numerical model to simulate the horizontal water entry of a cylinder with a low Froude number and revealed the effects of the cylinder's length, diameter, and speed on cavitation morphology. Liu et al. (2020) utilized the volume of fraction (VOF) method to investigate the oblique water entry of a cylinder; they found that high water entry speeds induced a secondary closure phenomenon in cavitation. Zhang et al. (2022) conducted numerical studies on a free interface during circular cylinder water entry and exit, using the immersed boundary–multiphase lattice Boltzmann flux solver. Sun et al. (2018) explored structural water entry issues using smoothed particle hydrodynamics.

Owing to advancements in technology and the diversification of application scenarios, intricate environmental boundaries have been encountered, including irregular fluid and limited-domain boundaries. A typical scenario involving irregular boundaries is the entry of structures into water under wave conditions (Wang and Wang, 2010). Another example involves the deployment of spacecraft on ice layers with prefabricated holes and the entry of missiles into water near marine reefs. Both examples fall under limited-domain boundaries. Complex environmental boundaries can result in differential multiphase fluid behavior, particularly the lag fluid–structure interaction effect caused by the unstable evolution of cavitation, which is an important topic and widely researched (Wang et al., 2021; Wang et al., 2023). However, few studies have addressed water entry into structures with limited-domain boundaries, and associated mechanical mechanisms require further investigation.

This study employs the Eulerian finite element method for fluid simulation. This method, initially proposed by Benson et al. (2004; 2008), offers significant advantages in addressing transient impact and large deformation problems. Tian et al. (2018) applied this method to study underwater explosion phenomena, effectively simulating complex multiphase flow characteristics, such as cavitation pulsation, and highlighting the evident strengths of numerical algorithms. Furthermore, the present study adopts an enhanced immersed boundary method to manage fluid–structure interaction interfaces. This method, developed initially to address cardiac blood flow problems (Peskin, 1972), avoids numerical challenges posed by body-fitted grids and is robust in handling significant deformation issues.

This study employs the Eulerian finite element method with an immersed boundary model to simulate water entry in a limited-domain water problem. The second section introduces the relevant cavitation theory. The third section explores specific numerical methods. The fourth section validates the effectiveness of the numerical simulation method on the basis of pneumatic water entry experiment results. Finally, fluid–structure interaction under initial conditions, including various structures' typical sizes and velocities, is comprehensively discussed.

2 Theoretical analysis

Preliminary calculations in theoretical research are conducted on structural motion equations and cavitation size, providing a foundation for establishing initial boundary parameters in the numerical simulation of relevant problems. Figure 1 illustrates the schematic of the cavitation solution, and the derivation process incorporates principles such as energy conservation. The detailed derivation process is presented in this section (Lee et al., 1997).

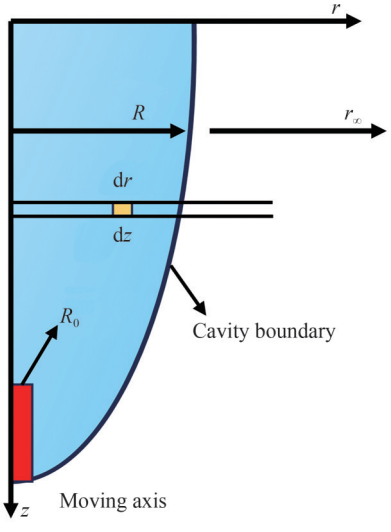

Figure 1 Schematic of structural water entry cavitation theory

Cavitation number (Hangen, 1999) is an essential parameter in the high-speed water entry of a structure and can be defined as follows:

$$\sigma = \frac{p - p_c}{\frac{1}{2}\rho_w v_p^2} \tag{1}$$

where p is the environmental pressure outside the cavitation, p_c is the pressure inside the cavitation, ρ_w is the density of water, and v_p is the speed of the structure. When the structure is in contact only with a free surface, the initial cavitation number $\sigma_0 = \frac{C_a \rho_a}{\rho_w}$ can be referred to in the literature, ρ_a is the density of air, and C_a is the air pressure drop coefficient. Under the initial conditions, the cavitation number can be obtained using the following equation (Lee et al., 1997):

$$\sigma = \sigma_0 \left(\frac{v_0}{v_p} \right)^2 \tag{2}$$

The following equation can derive the resistance coefficient C_d of a flat-head structure (Lee et al., 1997):

$$C_d = \mathrm{C}_0(1 + \sigma) \tag{3}$$

where C_0 is a constant, which can be 0.82.

If fluid motion is irrotational, it can be obtained through Bernoulli's equation and integration (Lee et al., 1997),

$$\left.\frac{\partial \varphi}{\partial t}\right|_R + \frac{\dot{R}}{2} = \frac{\Delta P}{\rho} + gz \tag{4}$$

where φ is the potential function, R is the cavitation radius size, g is the gravitational acceleration, ΔP is the pressure difference between the surrounding fluid and cavitation, and z is the distance at which the structure enters the water.

Through a series of formula derivations, the radius function of the cavitation is obtained as follows (Lee et al., 1997):

$$\begin{aligned} R^2 = R_0^2 + 2R_0 \sqrt{\frac{C_d}{2\ln\left(r_\infty / R\right)}}\left(z - z_0\right) - \\ \frac{\sigma}{2\ln\left(r_\infty / R\right)}\left(z - z_0\right)^2 - gz\left(t - t_0\right)^2 \end{aligned} \tag{5}$$

The maximum radius of the cavitation is obtained using the equation shown below (Lee et al., 1997). For instance, for the water entry of a structure traveling at 100 m/s, specific numerical values are used in estimating the maximum radius of the cavitation. The calculated value is approximately 6–10 times the radius of the flat bottom and provides essential theoretical support for boundary selection. The schematic of water entry cavitation in limited-domain water is depicted in Figure 2. When the radius of the water domain is significantly smaller than the theoretical maximum size of the cavitation in an infinite water domain, the corresponding cavitation shape is substantially influenced by the boundary.

$$R_m = R_0 \sqrt{\frac{C_d}{\sigma} + 1} \tag{6}$$

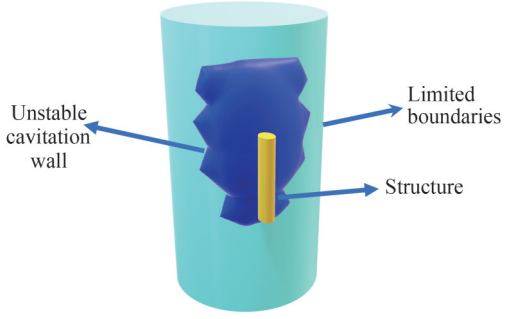

Figure 2 Schematic of water entry cavitation in a limited-domain water

3 Numerical method

3.1 Eulerian finite element method

Numerical simulations of axisymmetric models are conducted to enhance the efficiency of numerical simulations while maintaining solution accuracy. The compressible Eulerian finite element method offers significant advantages in addressing the transient large deformation problems of fluids, such as water entry. After the viscous term is neglected, the control equation for each element during the solving process is as follows (Benson and Okazawa, 2004; Benson, 2008):

$$\frac{\partial \varphi}{\partial t} = S \tag{7}$$

$$\frac{\partial \varphi}{\partial t} + \nabla \cdot \left(\varphi \boldsymbol{u}\right) = 0 \tag{8}$$

where $\boldsymbol{u} = \left\{u_r, u_z\right\}$ is the speed vector, φ is the undetermined variable, and S is the source term. The above equation is established in a cylindrical coordinate system, and r, θ, and z represent the radial, circumferential, and axial directions, respectively. Equations (7) and (8) are divided into Lagrangian and Eulerian steps through operator separation, which combines the advantages of Lagrangian and Euler descriptions. In addition, the equations of mass, momentum, and energy S and φ are expressed in different forms as follows:

$$\begin{cases} S = 0, & \varphi = \rho \\ S = p_i' - \rho g_i, & \varphi = \rho u_i \\ S = -p\nabla \cdot \boldsymbol{u}, & \varphi = \rho e_{\mathrm{in}} \end{cases} \tag{9}$$

where ρ is the density of the fluid, subscripts $i = 1, 2$ repre-

sent radial and axial directions, g_i is the gravitational acceleration, e_{in} is the internal energy per unit mass, i represents the direction of the partial derivative, and speed divergence $\nabla \cdot \boldsymbol{u} = \sum_{i=1}^{2} \frac{\partial u_i}{\partial x_i} + \frac{1}{r} u_r$.

The Lagrangian calculation step is the solution to Equation (7), and the explicit finite element method is used as the processing method. The following can be derived by integrating and stepwise transforming the momentum equation in cylindrical coordinates:

$$\iint_{\Omega} \rho \ddot{u}_i \phi \mathrm{d}s = -\int_{\Gamma} p \phi n_i \mathrm{d}l + \iint_{\Omega} \left[\rho g_i \phi + p \nabla \phi \right] \mathrm{d}s \tag{10}$$

where Ω is the discrete two-dimensional orthogonal computational domain, Γ is the boundary of the computational domain, n_i is the projection pointing toward an area outside the domain in the direction, and ϕ is the shape function. Integrating Equation (10) facilitates discrete solving. An explicit integral format is used to update fluid motion, and the mesh adapts to a fluid material, as described below.

$$u_i^{\left(n+\frac{1}{2}\right)} - u_i^{\left(n-\frac{1}{2}\right)} = a_i^{(n)} \Delta t \tag{11}$$

$$x_i^{(n+1)} - x_i^{(n)} = u_i^{\left(n+\frac{1}{2}\right)} \Delta t \tag{12}$$

The subscript represents the number of time steps and Δt is the length of the time steps. The material density and energy equations of the system must be solved using the following equation:

$$\frac{\mathrm{d}\rho}{\mathrm{d}t} + \rho(\nabla \cdot \boldsymbol{u}) = 0 \tag{13}$$

and

$$\frac{\mathrm{d}\rho e_{\text{in}}}{\mathrm{d}t} + \left(p + \rho e_{\text{in}} \right) \nabla \cdot \boldsymbol{u} = 0 \tag{14}$$

At this stage, the Lagrangian process for each calculation time step is completed, and the Eulerian calculation steps are initiated. The core concept of the Eulerian finite element method is determining the transport volume between elements with the VOF method and the monotonic upwind transport scheme. Another important concept is updating variables, such as momentum. Once a current time step involving Euler calculations is completed, the initial pressure and other variables for the following calculation steps are updated using the state equation. The iterative process of Lagrangian and Eulerian calculations facilitates the resolution of complex problems. The state equation is crucial. The Tammann equation is selected as the state equation for water and air (Tian et al., 2020) and expressed as follows:

$$p = \rho e_{\text{in}} \chi - \rho e_{\text{in}} - \chi P_w \tag{15}$$

where χ is adiabatic rate, P_w is the reference pressure, and e_{in} is unit fluid energy.

Table 1 Specific material constants for the equation of state

Material	P_w (MPa)	γ	ρ_0 (kg/m^3)
Water	330.9	7.15	1 000
Air	0	1.25	1.25

3.2 Immersed boundary method

For nonlinear fluid–structure interaction problems, interface treatment is relatively complex. The penalty function immersed boundary method is utilized to handle the unbalanced restriction of the boundary position (He et al., 2021; 2024). In numerical simulations, this method employs a relatively simple Cartesian grid, which prevents numerical divergence caused by body-fitted grids, modifies the control equation of the fluid element where the solid node is located, and introduces additional volume forces. The control equation is extended from the two-dimensional format to an axisymmetric one, where the physical force comprises the combined forces of the additional volume force and gravity. The following equation represents the momentum equation of the fluid element at the solid boundary node and is applicable to all immersed boundary methods.

$$\frac{\partial \rho \boldsymbol{u}}{\partial \boldsymbol{t}} + \nabla \cdot \left(\rho \boldsymbol{u} \boldsymbol{u} \right) + \nabla \boldsymbol{p} = \boldsymbol{f}^{\boldsymbol{c}} + \rho \boldsymbol{g} \tag{16}$$

The condition of fluid–structure interaction is achieved and solved through repeated iterations of immersion depth by introducing volume force $\boldsymbol{f}^{\boldsymbol{c}}$ through the interface. This model enhances the mathematical formula for immersion depth in strongly nonlinear problems, such as water entry. Based on the original equation, a damping force term is added to improve the stability of numerical simulations. This adjustment ensures improved performance for complex scenarios.

$$\boldsymbol{f}^{\text{RB}} = -\kappa \varepsilon \boldsymbol{n} - C \dot{\varepsilon} \boldsymbol{n} \tag{17}$$

$$\varepsilon^{n+1} = \varepsilon^n + \Delta t \left(\boldsymbol{u}^b - \sum_{m=1}^{4} \phi_m \boldsymbol{u}_m \right) \cdot \boldsymbol{n} \tag{18}$$

$$\dot{\varepsilon} = \frac{\varepsilon^{n+1} - \varepsilon^n}{\Delta t} = \left(\boldsymbol{u}^b - \sum_{m=1}^{4} \phi_m \boldsymbol{u}_m \right) \cdot \boldsymbol{n} \tag{19}$$

$$\boldsymbol{f}^{\boldsymbol{c}} = -\phi_m \boldsymbol{f}^{\text{RB}} (m = 1{:}4) \tag{20}$$

where κ is the penalty stiffness coefficient, $\boldsymbol{f}^{\text{RB}}$ is the total interface force, ε is the immersion depth, $\boldsymbol{u}^b$ is the speed of the contact boundary node, $\boldsymbol{n}$ is the normal vector, $\boldsymbol{u}_m$ is the node speed of the fluid element where the solid boundary node is located, ϕ_m is the shape function of node m, and C is the damping coefficient. Figure 3 illustrates the

schematics of the Eulerian finite element and penalty function immersed boundary methods, where the core processing methods in the model can be intuitively seen.

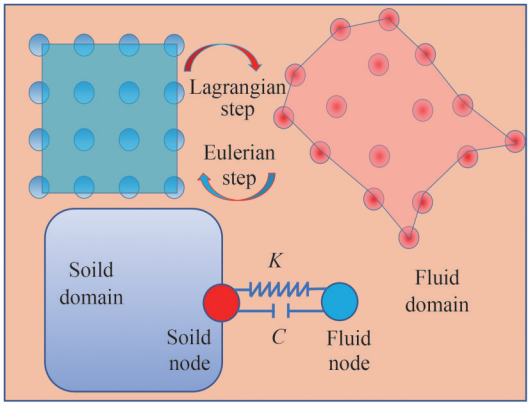

Figure 3 Schematics of the Eulerian finite element and penalty function immersed boundary methods

4 Experimental verification

The numerical model is validated through experiments, and the water entry experimental device used is depicted in Figure 4. The primary method is controlling the free fall of the structure through air pressure regulation. Compared with the magnetic control method, the pneumatic method allows the structure to fall vertically instantaneously, mitigating the influence of initial disturbances on the water entry's initial state. The pneumatic device comprises an oil-free air compressor, a control valve, an air purification device, a gas pipe, and a sucker. The water tank used in the experiment has dimensions of 40 cm × 60 cm × 80 cm, is fixed, and provides a water entry speed for the projectile through a supporting structure. High-speed cameras are utilized to capture the evolution of the entire physical process.

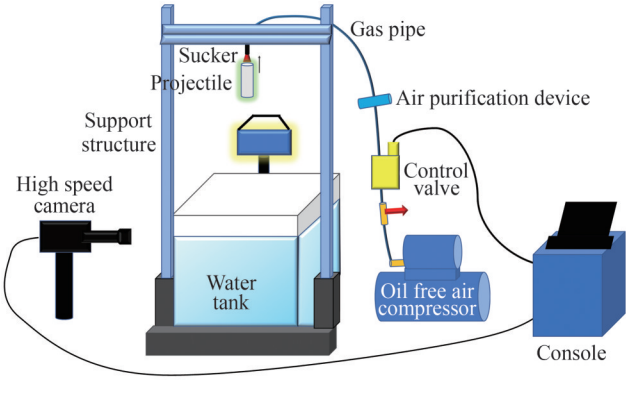

Figure 4 Diagram of the water entry experimental device

Figure 5 presents the results of the experiment on an acrylic cylindrical projectile, which is 16 cm in length and 4 cm in bottom diameter, while it enters water. Complete cavitation evolution is thoroughly examined on the basis of experimental results. When t = 1.04 ms, the projectile structure just touches the water surface, and the fluid motion at the free surface is insignificant. At t values of 6.08 and 9.80 ms, cavitation emerges in the lower part of the projectile structure, causing movement in the surrounding flow field. Under this condition, the cavitation does not close during the early stage of the projectile's movement but encases both sides of the projectile, particularly when t = 24.8 ms. The projectile does not fully enter the water until t = 38.6 ms. At this point, the pulsation of the cavitation wall becomes distinct, and a cavitation region reappears at the tail of the projectile structure. Owing to the pressure in the flow field and the delayed motion of the cavitation wall, when t = 68.6 ms, the cavitation above the projectile displays a collapse trend. Accordingly, the initial water entry cavitation size is relatively small at this stage.

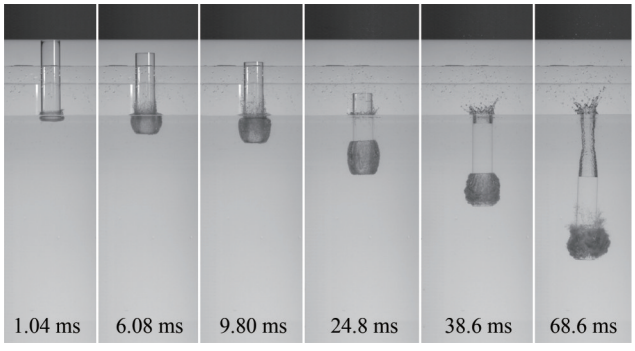

Figure 5 Results of a 5.86 m/s cylindrical water entry experiment

A cylindrical acrylic container with a diameter of 55 mm is positioned directly beneath the structure. Based on the experimental conditions, the limited-domain boundary conditions are established. Figure 6 presents the experimental results of a cylindrical projectile entering the limited-domain water. The impact of each boundary effect on cavitation evolution is effectively investigated. When t = 3.40 ms, the projectile structure touches the free surface, and the boundary effect on the initial cavitation is relatively minor. When t = 35.50 ms, the entire structure of the projectile is enveloped by cavitation, and the fluid surrounding the structure undergoes intense motion. Unlike when conditions are devoid of boundary constraints, the restriction of water bodies intensifies the formation and evolution of cavitation, significantly increasing the size of the incoming cavitation. As the projectile structure descends, a waveform trend emerges on the cavitation wall, becoming increasingly pronounced. The numerical results corroborate this phenomenon. A comparison of Figures 6 and 7 reveals the one-to-one correspondence between the time in the experimental results and the time in the numerical results, aligning precisely simultaneously. In the numerical simulation process of validation condition, the size of the computational domain and other parameters are consistent with the experimental parameters, and the minimum size of the grid is 0.001 m.

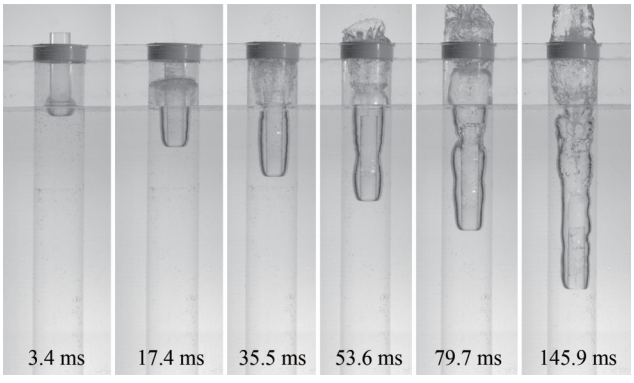

Figure 6 Results of a 5.86 m/s cylindrical water entry in a limited-domain experiment

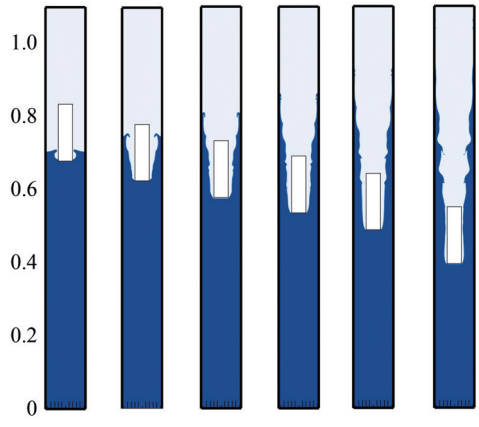

Figure 7 Numerical results of a 5.86 m/s cylindrical water entry in the limited-domain experiment

Figure 8 highlights substantial discrepancies in the attenuation of the water entry speed of the structure under different boundary conditions. The flow field evolution is more intense in small computational domains, and the structure's kinetic energy is readily converted into fluid kinetic energy. Hence, structural speed attenuation is rapid. As for large computational domains, the pulsating load's robust nonlinearity, which is due to incomplete cavitation opening and pulsation around the structure, results in nonlinearity in the structural speed evolution. Accordingly, numerical simulation algorithms successfully model the influence of boundary effects on cavitation evolution during water entry and have good convergence. This study conducts comprehensive studies using numerical methods on the basis of these findings.

5 Results and discussion

5.1 Influence of structural size

In a flow field environment in an infinite water domain, structure size, encompassing cavitation size and cavitation

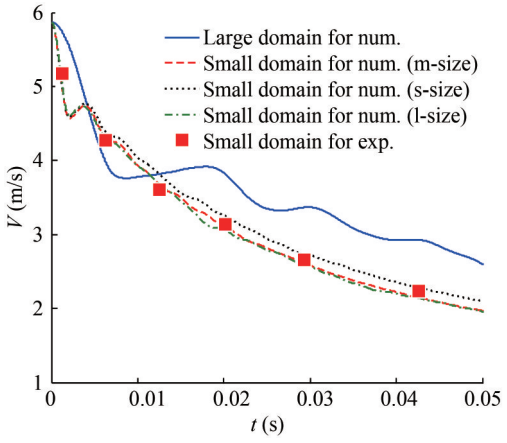

Figure 8 Attenuation curve of the water entry speed of the structure under different boundary conditions and a comparison of the numerical and experimental results

closure time, is a critical factor influencing fluid–structure interaction. By contrast, studies on a limited water domain have not been conducted, and the effect of structural size remains unclear. This study introduces the concept of restriction ratio, focusing on a structure with a flat-headed rotating body and using the diameter of the structure's bottom edge as the characteristic length. The restriction ratio, defined as the ratio of the bottom boundary size of the water domain to the bottom boundary size of the structure, is used in explaining the physical mechanism of this process. The evolution of free surfaces and structural speed attenuation are then explored using various parameters.

Figure 9 demonstrates a considerable difference in the water entry process among structures with varying structural restriction ratios, which are reflected in the distinct characteristics of cavitation evolution. When the structural restriction ratio is 5.5, the cavitation morphology exhibits different typical characteristics at various time points. At t values of 0.005–0.062 s, water entry is in the opening cavitation stage, and as the structure moves, the cavitation shape changes, showing a clear correlation with the structure's size. When t = 0.08 s, cavitation undergoes surface closure because of the radial motion of the free surface. When t = 0.146 s, the evolution of cavitation enters the later stage, exhibiting complex phenomena, such as collapse and tearing. When the structural restriction ratio is 1.83, the structure's motion results in a relatively continuous open cavitation stage, and all instances shown in the figure occur during this stage. As the structure moves, the free surface climbs upward along the wall, and the local unstable motion of the inner wall of the cavitation becomes more apparent. Figure 10 reveals that a small structural size results in large initial speed attenuation. However, a nonlinear characteristic emerges during the later stage of speed attenuation, where a moderate structural size leads to slower attenuation. This behavior is attributed to the complex fluid–

structure interaction response associated with the cavitation effect.

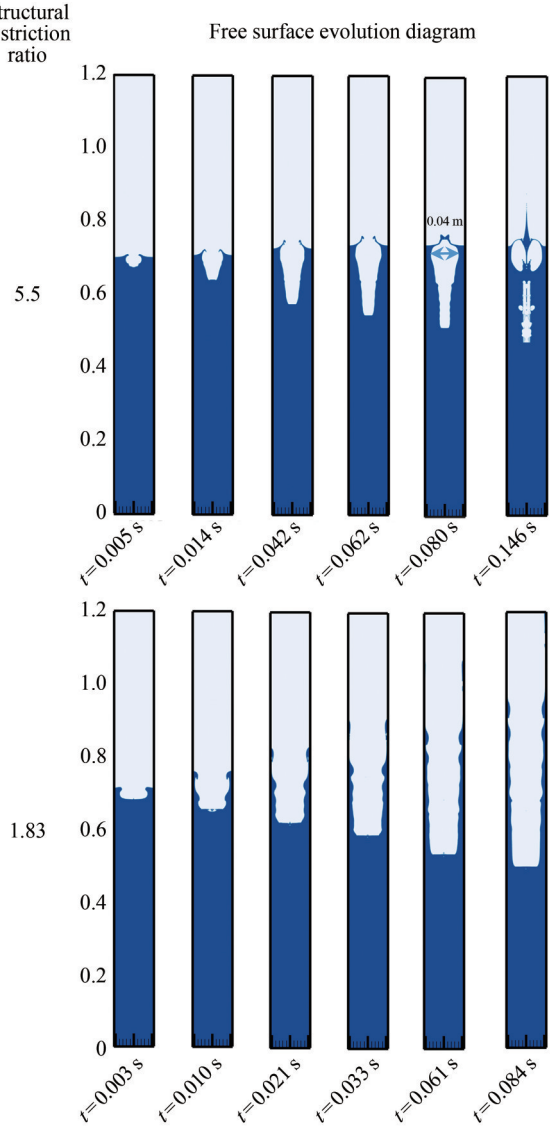

Figure 9 Evolution diagram of a free surface in structures with different structural restriction ratios during water entry

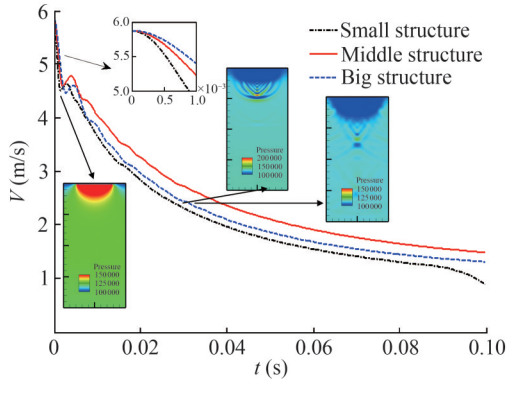

Figure 10 Evolution diagram of water entry speed for structures with different structural sizes (Typical pressure field is labeled)

5.2 Influence of water domain size

The restriction ratio is determined by structural and water domain size. The preceding section primarily examines the impact of structural size. This section maintains the structural size constant and investigates the evolving flow field mechanisms caused by variations in water domain size. The critical parameter is the characteristic size of the water domain under limited conditions. For axisymmetric models, modifying the bottom diameter of the water domain is sufficient to alter its characteristic size. Reducing the characteristic size of the water domain changes boundary effects, influencing fluid–structure interaction, although the specific mechanical phenomena involved are complex. The physical mechanism of this process is qualitatively analyzed by examining the evolution of the free surface, structural speed attenuation, and structural acceleration at different parameters.

Figure 11 illustrates differences in the water entry of structures with various water restriction ratios, showing distinct fundamental characteristics in cavitation evolution. At a water restriction ratio of 3.3, specific features emerge in the cavitation morphology at different time points. At t values of 0.003–0.119 s, water entry remains in the opening cavitation stage, and the cavitation shape evolves as the structure moves. When t = 0.152 s, owing to the radial motion of the free surface, cavitation closure occurs, accompanied by a closure time that is significantly delayed as compared with that in Figure 9. At this stage, fluid motion along the boundary causes the free surface head to appear relatively slender. When the structural restriction ratio is 2.2, the structure's motion leads to a continuous opening cavitation stage. As the structure progresses, the free surface rises along the wall, and the local unstable motion of the cavitation's inner wall becomes prominent. At t of 0.196 s, the cavitation exhibits a deep closure phenomenon, and the structure is almost entirely enveloped by water.

Figure 12 demonstrates that the speed attenuation of the structure remains consistent initially at varying water domain sizes. However, as the boundary fluid begins to move, variations in speed attenuation occur. When the water domain is small, a more pronounced decrease in structural speed occurs over time. This phenomenon can be attributed to a boundary confinement effect that restricts fluid movement and increases vertical kinetic energy. In addition, the structure's motion can be divided into three stages, which correspond to distinct fluid–structure interaction mechanisms. An analysis of the acceleration evolution curve reveals that the peak impact acceleration when the structure enters the water remains relatively constant under the three depicted working conditions. This consistency shows that discrepancies in speed attenuation are caused by complex fluid motion, which leads to subsequent load pulsation.

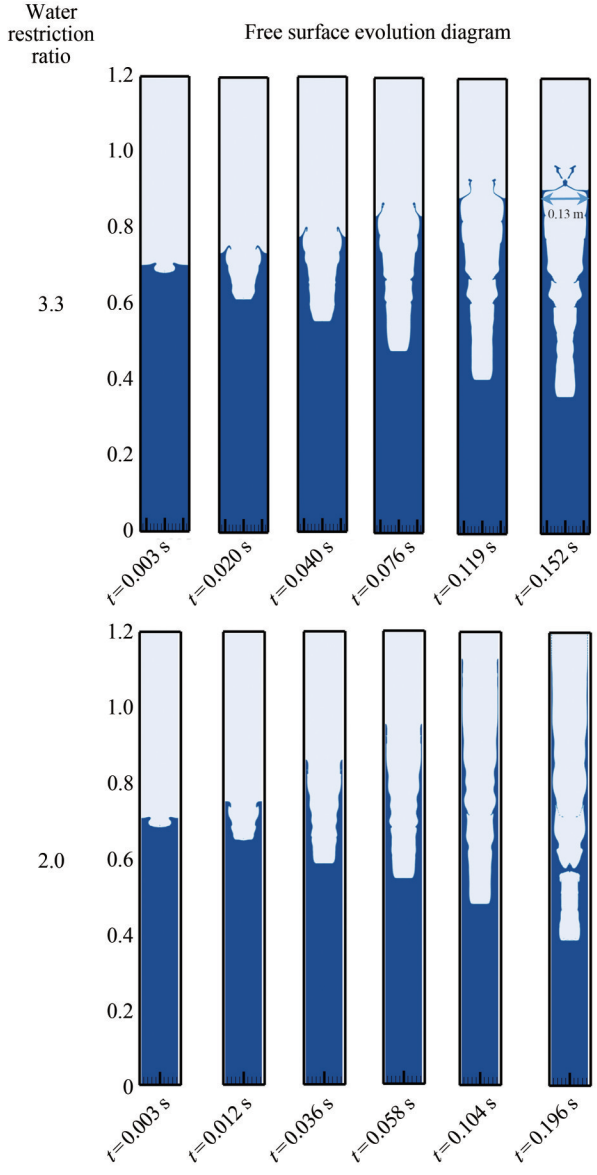

Figure 11 Evolution diagram of free surface for structures with different water restriction ratios during water entry

5.3 Influence of water entry speed

Speed is a critical factor influencing fluid–structure interaction. In general, high water entry speeds result in pronounced fluid–structure interaction effects. Safety risks and technical challenges in experiments are associated with structural water entry in confined water domains, including potential collisions between structures and walls. In real-world engineering applications, water entry speeds for structures vary considerably, and projectile structures typically enter at speeds of tens of meters per second. This finding highlights the distinct benefit of numerical calculations in such scenarios. The influence mechanism can be analyzed by simply adjusting the water entry speed. A qualitative understanding of the physical mechanism of this process

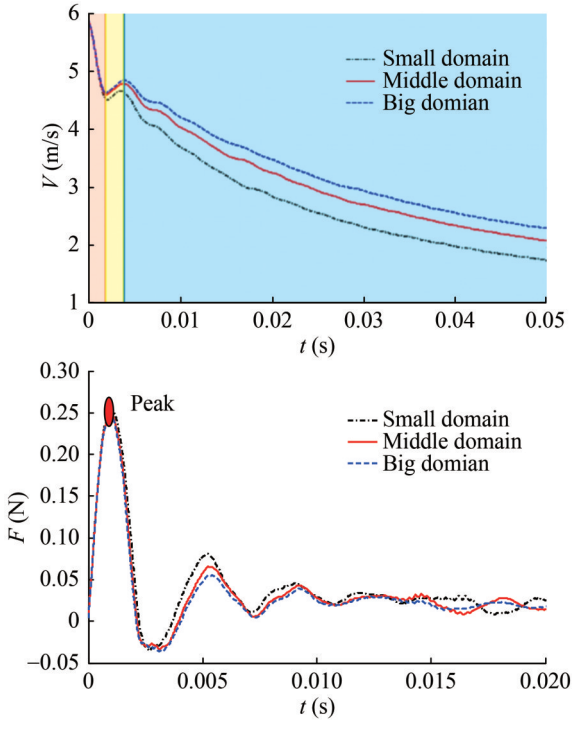

Figure 12 Evolution diagram of water entry speed and acceleration of structures with different water domain sizes

can be achieved by using different parameters to observe the evolution of free surfaces and structural speed attenuation. Speed values undergo dimensionless processing based on the initial speed to facilitate accurate analysis.

Figure 13 indicates considerable differences in water entry of structures at varying water entry speeds. At relatively high water entry speeds, the overall trend of cavitation evolution tends to remain consistent. When the structure's speed is 11.72 m/s, the evolution of the cavitation morphology exhibits distinct characteristics at different times. However, at t values of 0.003–0.08 s, water entry is in the stage of opening cavitation. As the structure moves, the shape of the cavitation becomes increasingly complex, and the corresponding surface instability of the cavitation intensifies. When the water entry speed of the structure is 46.3 m/s, the structure's motion leads to a relatively continuous stage of opening cavitation, and all moments in the figure fall within this stage. However, the longer the overall length of the cavitation, the stronger the surface instability of the cavitation. Figure 14 shows that the initial dimensionless speed attenuation is generally consistent when the speed changes, although speed attenuation changes after the fluid boundary motion is completed. In the later stage, the smaller the water entry speed of the structure, the lower the corresponding nondimensional speed attenuation efficiency. By contrast, the greater the water entry speed of the structure, the more pronounced the fluctuations in the speed curve.

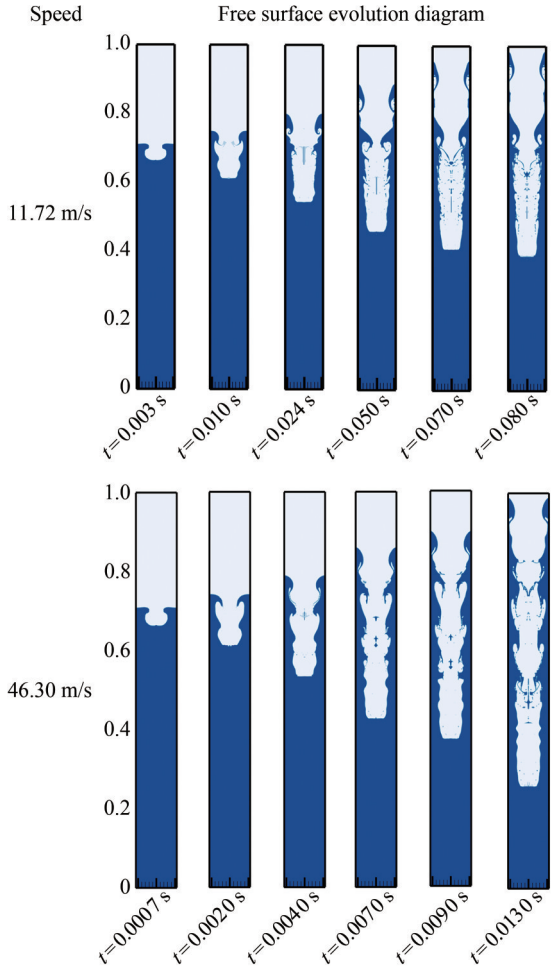

Figure 13 Evolution diagram of free surface for structures with different water entry velocities

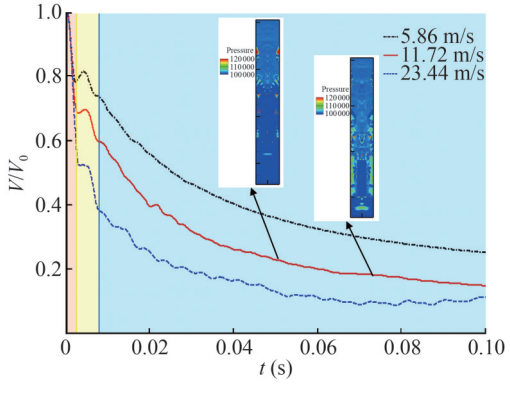

Figure 14 Evolution diagram of dimensionless speed for structures with different water entry velocities (a typical pressure field is labeled)

6 Conclusions

This study employs the Eulerian finite element method for fluid simulation and utilizes an improved immersed boundary method to address fluid–structure interaction interfaces. A coupling numerical model is developed for water entry in limited-domain water. First, a water entry cavitation theory is derived, and the approximate range of boundary effects is presented. The numerical model is then validated through structural water entry experiments with pressure regulation. The results demonstrate the effectiveness of the numerical algorithm. Hence, a series of in-depth studies is conducted using numerical methods to analyze the effects of structural size, water domain size, and water entry speed. The following conclusions can be drawn:

1) Considerable differences are observed in the water entry of structures with varying structural restriction ratios, reflecting the distinct basic characteristics of cavitation evolution. When the structural restriction ratio is 1.83, the motion of the structure results in a relatively continuous open cavitation stage. As the structure moves, the free surface continuously climbs upward along the wall, and the local unstable motion of the inner wall of the cavitation becomes pronounced. Smaller structural sizes exhibit considerable initial speed attenuation, with later speed attenuation demonstrating nonlinear characteristics.

2) When the water domain size is small, the later structural speed attenuation becomes prominent because of the boundary confinement effect, which restricts fluid movement and generates a large amount of vertical kinetic energy. The cavitation exhibits a deep closure phenomenon when the structural restriction ratio is 2.2. Furthermore, the movement of structures in limited-domain water can be categorized into three stages, which correspond to distinct fluid–structure interaction mechanisms.

3) When the water entry speed varies, the initial dimensionless speed attenuation remains consistent, but speed attenuation changes after the completion of fluid boundary motion. In the later stage, low water entry speeds correspond to low nondimensional speed attenuation efficiency. High water entry speeds result in pronounced fluctuations in the speed curve. In these cases, the overall cavitation length increases, and the surface instability of the cavitation is pronounced.

This article adopts an axisymmetric model and only conducts a relatively systematic study on the problem of vertical water entry for cylinders. Some basic fluid–structure interaction mechanisms have been discovered, but asymmetric phenomena cannot be revealed yet, which will be examined in our future research.

Funding Supported by the National Natural Science Foundation of China under Grant Nos. 52401312, 38021746 and 12202011, China Postdoctoral Science Foundation under Grant No. 2023M740036 and 2022M710190, and the Postdoctoral Fellowship Program of CPSF under Grant No. GZC20240014.

Competing interest The authors have no competing interests to declare that are relevant to the content of this article.

References

Aristoff JM, Bush JWM (2009) Water entry of small hydrophobic spheres. Journal of Fluid Mechanics 619: 45-78. DOI: 10.1017/S0022112008004382

Benson DJ (2008) Momentum advection on unstructured staggered quadrilateral meshes. International Journal for Numerical Methods in Engineering 75(13): 1549-1580. DOI: 10.1002/nme.2310

Benson DJ, Okazawa S (2004) Contact in a multi-material Eulerian finite element formulation. Computer Methods in Applied Mechanice and Engineering 193(39/41): 4277-4298. DOI: 10.1016/j.cma.2003.12.061

Gekle S, Peters I, Gordillo JM, Meer DVD, Lohse D (2009) Supersonic air flow due to solid-liquid impact. Physical Review Letters 104(2): 024501. DOI: 10.1103/PhysRevLett.104.024501

Hangen N (1999) Correction of incipient cavitation number for scale effect. Journal of Hydraulic Engineering 30(9): 28-32. DOI: 10.3321/j.issn:0559-9350.1999.09.005

He M, Liu YL, Ren SF, Liu WT (2021) The nonlinear coupling of oscillating bubble and floating body with circular hole. Computer Modeling in Engineering & Sciences 127(3): 923-942. DOI: 10.32604/cmes.2021.015259

He M, Yan JL, Lv PY, Duan HL, Zhang AM (2024) Research on ice-breaking characteristics of underwater explosion bubbles based on an effective coupled model. Applied Ocean Research 153: 104259. DOI: 10.1016/j.apor.2024.104259

Howison SD, Ockendon JR, Wilson SK (1991) Incompressible water-entry problems at small deadrise angles. Journal of Fluid Mechanics 222: 215-230. DOI: 10.1017/S0022112091001076

Huang XT, Sun PN, Lyu HG, Zhang AM (2022) Water entry problems simulated by an axisymmetric SPH model with vas scheme. Journal of Marine Science and Application 21(2): 1-15. DOI: 10.1007/s11804-022-00265-y

Iranmanesh A, Passandideh-Fard M (2017) A three-dimensional numerical approach on water entry of a horizontal circular cylinder using the volume of fluid technique. Ocean Engineering 130: 557-566. DOI: 10.1016/j.oceaneng.2016.12.018

Karman TV (1929) The impact of seaplane floats during landing. National Advisory Committee for Aeronatics, technical note No. 321, 309-313

Lee M, Longoria R, Wilson D (1997) Cavity dynamics in high-speed water entry. Physics of Fluids 9(3): 540-550. DOI: 10.1063/1.869472

Liu H, Zhou B, Han XS, Zhang T, Zhou BK, Gho WM (2020) Numerical simulation of water entry of an inclined cylinder. Ocean Engineering 215: 107908. DOI: 10.1016/j.oceaneng.2020. 107908

Logvinovich GV (1969) Hydrodynamics of flows with free boundaries. Naukova Dumka, Kiev, 216 pp

Peskin CS (1972) Flow patterns around heart valves: a numerical method. Journal of Computational Physics 10(2): 252-271. DOI: 10.1016/0021-9991(72)90065-4

Prasad BS, Sastry GRK, Das HN (2024) A comprehensive review study on multiphase analysis of water entry bodies. Ocean Engineering 292: 116579. DOI: 10.1016/j.oceaneng.2023.116579

Sun PN, Zhang AM, Marrone S, Ming FR (2018) An accurate and efficient SPH modeling of the water entry of circular cylinders. Applied Ocean Research 72: 60-75. DOI: 10.1016/j.apor.2018.01.004

Tian ZL, Liu YL, Zhang AM, Tao LB (2020) Energy dissipation of pulsating bubbles in compressible fluids using the Eulerian finite-element method. Ocean Engineering 196: 106714. DOI: 10.1016/j.oceaneng.2019.106714

Tian ZL, Liu YL, Zhang AM, Wang SP (2018) Analysis of breaking and re-closure of a bubble near a free surface based on the Eulerian finite element method. Computers & Fluids 170: 41-52. DOI: 10.1016/j.compfluid.2018.04.028

Truscott TT, Epps BP, Belden J (2014) Water entry of projectiles. Annual Review of Fluid Mechanics 46(1): 355-378. DOI: 10.1146/annurev-fluid-011212-140753

Truscott TT, Techet AH (2009) Water entry of spinning spheres. Journal of Fluid Mechanics 625: 135-165. DOI: 10.1017/S0022112008005533

Wagner H (1932) Phenomena associated with impacts and sliding on liquid surfaces. Mathematics and Mechanics 12(4): 193-215

Wang WH, Wang YY (2010) Numerical study on cylinder entering water in wave. Journal of Shanghai Jiao Tong University 44(10): 1393-1399

Wang ZY, Cheng HY, Ji B (2021) Euler–Lagrange study of cavitating turbulent flow around a hydrofoil. Physics of Fluids 33(11): 112108. DOI: 10.1063/5.0070312

Wang ZY, Cheng HY, Ji B, Peng XX (2023) Numerical investigation of inner structure and its formation mechanism of cloud cavitating flow. International Journal of Multiphase Flow 165: 104484. DOI: 10.1016/j.ijmultiphaseflow.2023.104484

Worthington AM, Cole RS (1899) Impact with a liquid surface, studied by the aid of instantaneous photography. Paper II. Proceedings of the Royal Society of London 65: 153-154. DOI: 10.1098/rspl.1899.0014

Yuan XL, Wang YD, Zhu Z (2012) Experimental investigation on hydrodynamic characteristics of supercavitating vehicles. 8th International Symposium on Cavitation. DOI: 10.3850/978-981-07-2826-7_087

Zhang AM, Li SM, Xu RZ, Pei SC, Li S, Liu YL (2024) A theoretical model for compressible bubble dynamics considering phase transition and migration. Journal of Fluid Mechanics 999: A58. DOI: 10.1017/jfm.2024.954

Zhang GY, Yan HR, Song H, Wang H, Hui D (2022) Numerical investigation on the deformation of the free interface during water entry and exit of a circular cylinder by using the immersed boundary-multiphase lattice Boltzmann flux solver. Journal of Marine Science and Application 21(3): 99-113. DOI: 10.1007/s11804-022-00292-9

Zhang Q, Zong Z, Sun TZ, Yu YQ, Li HT (2021) Characteristics of cavity collapse behind a high-speed projectile entering the water. Physics of Fluids 33(6): 062110. DOI: 10.1063/5.0053409

Zhang YQ, Xu F, Cai WJ, Li JC (2017) Experimental study on the impact response of different structures water entry. International Conference on Mechanical & Aerospace Engineering, 644-647. DOI: 10.1109/ICMAE.2017.8038723

Zou W, Gan H (2024) Free motion characteristics of the ventilated supercavitating vehicles. Journal of Physics: Conference Series 2756: 012046. DOI: 10.1088/1742-6596/2756/1/012046